Photoionization and fragmentation of H_3O^+ under XUV irradiation

C. Domesle,[1] S. Dziarzhytski,[2] N. Guerassimova,[2] L. S. Harbo,[3] O. Heber,[4] L. Lammich,[3] B. Jordon-Thaden,[1] R. Treusch,[2] A. Wolf,[1] and H. B. Pedersen[3,*]

[1]*Max-Planck-Institut für Kernphysik, D-69117 Heidelberg, Germany*

[2]*DESY, Hamburg, Germany*

[3]*Department of Physics and Astronomy, Aarhus University, DK-8000 Aarhus C, Denmark*

[4]*Department of Particle Physics, Weizmann Institute of Science, Rehovot 76100, Israel*

(Received 30 July 2013; published 4 October 2013)

The photolysis of the hydronium cation H_3O^+ has been studied at the extreme ultraviolet wavelengths of 35.56 ± 0.24 nm (34.87 ± 0.24 eV) and 21.85 ± 0.17 nm (56.74 ± 0.44 eV) using a crossed ion-photon beam setup at the free-electron laser FLASH. Coincidence photoelectron and photofragment spectroscopy was performed at 21.85 nm, where both inner and outer valence ionization are allowed, and revealed that the XUV photolysis of H_3O^+ is by far dominated by ionization of outer valence electrons forming the $^1A_1$ and ^2E states of the dication H_3O^{2+}. The dications were found to dissociate into the channels $H_2O^+ + H^+$ ($72 \pm 4\%$), $OH^0 + 2H^+$ ($18 \pm 6\%$), and $OH^+ + H^+ + H^0$ ($10 \pm 1\%$). A kinematic analysis of the $H_2O^+ + H^+$ channel after photoabsorption at 35.56 nm (where only outer valence ionization is possible) showed dissociation into excited states of the water radical ion, where the $^1A_1$ state breaks up into the linear $\tilde{A}\,^2A_1$ state of H_2O^+ and the ^2E state decays into the strongly bent $\tilde{B}\,^2B_2$ state. Finally, from the ^2E state of H_3O^{2+}, dissociation into $OH^0(X\,^2\Pi) + 2H^+$ was identified to occur with a near linear dissociation geometry.

DOI: 10.1103/PhysRevA.88.043405 PACS number(s): 33.80.Eh, 33.80.Gj

I. INTRODUCTION

From spectroscopic observations [1–6], the hydronium ion H_3O^+ is known to exist in various interstellar environments, and chemical models of such environments [7–13] predict it to be a central oxygen-carrying ion. It is believed to be formed through a sequence of hydrogen additions to O^+, OH^+, and H_2O^+ through reactions with H_2, and destroyed by dissociative recombination with low-energy electrons. This is, for instance, formulated explicitly in models of so-called photon-dominated regions (PDRs) [9,10], occurring where interstellar clouds are exposed to far ultraviolet radiation (6–13.6 eV), and for regions exposed to x rays [11,12]. Additionally, the presence of H_3O^+ and higher water hydrate ions $H^+(H_2O)_n$ in the earth's ionosphere [14] as well as other planetary atmospheres [15] is well known. In the earth's ionosphere, for example, water cluster ions are formed through a complex chemistry initiated by molecular ionization by high-energy solar photons or cosmic rays. Interestingly, except for a single recent study [25], the photochemistry of the hydronium ion in the extreme ultraviolet (XUV) range, where valence ionization is possible, is experimentally unexplored and its consequences for models of atmospheric and astrophysical plasmas are essentially not understood.

We report here a detailed experimental study of photoionization and fragmentation of H_3O^+ in the XUV range using an experimental setup where isolated fast-moving ions are irradiated with intense pulses from a free-electron laser (FEL) and where all emerging photofragments—neutrals, photoions, and photoelectrons—can be detected in coincidence.

The ground state of H_3O^+ has been studied experimentally in great detail in spectroscopy; see, e.g., Ref. [16–18], and has similarly been addressed in several calculations, see e.g. Refs. [19–21]. Excited states of hydronium have been investigated both with *ab initio* calculations [22,23] and calculations on electron impact [24]. With the present experiment, we address directly the dynamics of the potential energy surfaces (PESs) of the *dicationic* (H_3O^{2+}) states reachable by vertical transitions from the ground state of the monocation.

The energy regime for photoinduced dynamics of the H_3O^+ system through valence electron ionization in the XUV regime is illustrated in Fig. 1. Through the Franck-Condon principle, the nuclear conformations of the resulting fragmenting dications H_3O^{2+} are governed by the conformation of the ground-state monocation. Its $X\,^1A_1$ ground state has a pyramidal structure (C_{3v}) with an OH bond length of $\sim$1.84 a.u. and an angle of $\angle$HOH $\sim 111.6^\circ$ [16,17,19,20]. This state is characterized by the electron configuration $(1a_1)^2(2a_1)^2(1e)^4(3a_1)^2$ and both outer valence ($1e$ and $3a_1$) and inner valence ($2a_1$) orbitals are accessible for ionization in the XUV regime. In a previous exploratory study [25] performed at the FLASH facility [26,27], we studied the photolysis of H_3O^+ at a wavelength of 13.5 nm (91.8 eV). The data described in Ref. [25] indicated that the XUV photoabsorption of H_3O^+ proceeds by electron ejection mainly from the outer valence orbitals ($3a_1$ and $1e$), whereafter the formed dications follow dissociative paths into both two-body $H_2O^+ + H^+$ and three-body $OH + 2H^+$ channels. However, the results presented in Ref. [25] were obtained with relatively low statistics, and it was not explicitly demonstrated that outer valence electrons were indeed ejected. Moreover, especially the possibly emerging heavy photoions (O^+, OH^+, and H_2O^+) could not be analyzed directly.

The experimental arrangement has been significantly improved [28,29] and now allows coincidence detection of *all* photoproducts, i.e., electrons and neutral as well as charged fragments. We present fragmentation data obtained both at $\lambda_1 = 21.85 \pm 0.17$ nm ($E_1 = 56.74 \pm 0.44$ eV), where both

*Author to whom all correspondence should be addressed: hbjp@phys.au.dk

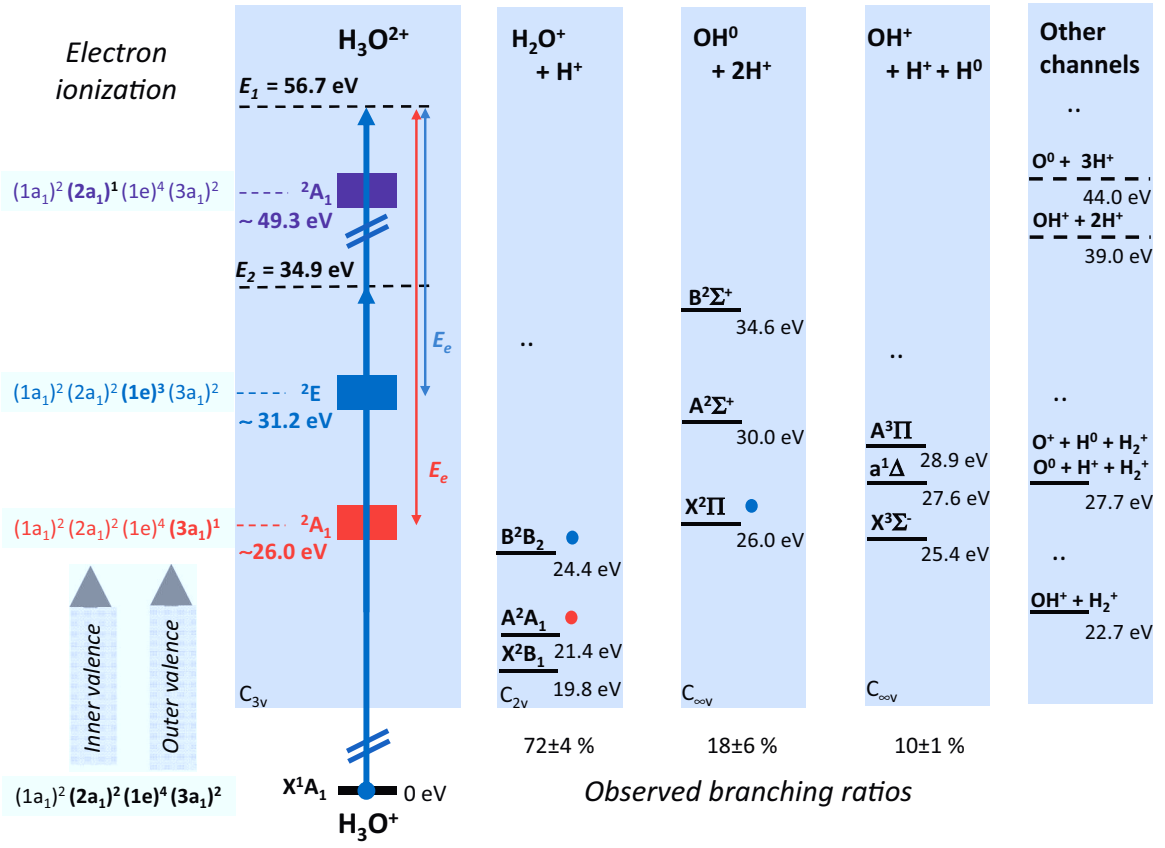

FIG. 1. (Color online) Illustration of the fragmentation channels accessible after valence shell photoionization of the hydronium ion (H_3O^+) at the applied XUV energies (E_1 and E_2). Calculated potential energy surfaces for the dication (H_3O^{2+}) electronic states in the Franck-Condon region of the ground state of H_3O^+ are not available; the energetic position of these states is estimated from the calculated orbital energies of H_3O^+ [23] and Koopmans' theorem [32]. The energies of the fragmentation limits are derived from data available at NIST [33]. The blue dot (at $B\,^2B_2$ and $X\,^2\Pi$) and the red dot (at $A\,^2A_1$) mark final states identified after ionization into the ^2E and $^2A_1$ states of H_3O^{2+}, respectively.

inner and outer valence ionization are energetically possible (see Fig. 1), and at $\lambda_2 = 35.56 \pm 0.24$ nm ($E_2 = 34.87 \pm 0.24$ eV), where for energetic reasons only outer valence electrons can contribute to the ionization.

At the shorter wavelength (λ_1) we detect the released photoelectron and specify its energy, explicitly demonstrating that outer valence ionization is by far the dominating ionization channel; by detection of the atomic and molecular fragments, we analyze the branching of the dication into $H_2O^+ + H^+$, $OH^0 + 2H^+$, and $OH^+ + H^+ + H^0$. For the longer wavelength (λ_2), we report a kinematic analysis of the fragmentation on the populated excited potential energy surfaces of the H_3O^{2+} dications. We interpret the obtained fragment energy distributions as evidence for two-body dissociation of H_3O^{2+} producing electronically excited water radical ions while we identify three-body dissociation as yielding OH^0 molecules in their electronic ground state.

II. EXPERIMENT

A. Ion and photon pulses

The experiments were carried out at the ion beam setup TIFF (Trapped Ion Fragmentation with an FEL) [25,29] installed at the Plane Grating monochromator (PG2) beam line [30] of the Free Electron LASer in Hamburg (FLASH) facility [26,27] at Deutsches Elektronen Synchrotron (DESY).

Water cluster ions were produced in a hollow cathode ion source located on a high voltage platform, operated with a gas inlet of pure water vapor with an approximate pressure of 0.1 mbar, sustaining a discharge of 590 V and 24 mA and cooling the wall of the ion source to ca. ~30 °C. By extraction to the ground potential, a fast beam of ions with kinetic energy $E_0 = 4.2$ kV was generated, and the H_3O^+ ions were mass-selected by passing the beam through a magnetic bending field.

The H_3O^+ beam was electrically guided and shaped by apertures and slits before entering the crossed beam interaction zone as an essentially parallel beam of ~70 nA (linear ion density $\sim 2 \times 10^4$ cm^{-1}). During the measurement, the ion beam was chopped [25] into trains of 50 pulses each with a width of 1.5 μs and matching the time structure of the photon beam from FLASH. After the interaction region, the ion pulses were electrically deflected into a beam dump.

The FLASH facility delivered horizontally polarized radiation pulses at wavelengths 35.56 ± 0.24 nm and 21.85 ± 0.17 nm with a repetition rate of 10 Hz in the form of trains of 50 individual pulses spaced by 5 μs, each having <250 fs full width at half-maximum temporal width and an average energy of 41 μJ (34 μJ) at 35.56 nm (21.85 nm), respectively,

before entering the PG2 beamline. The photon pulses were guided through the PG2 beamline with the monochromator operated in zeroth order, resulting in an overall transmission of $T_{PG2} = 0.5 \pm 0.1$, to the crossed ion-photon interaction zone located about 1.5 m before the photon beam focus.

Before and after the interaction region, the photon beam was collimated with slits of 3×3 mm to ensure alignment with the electrode structure of the interaction region, suppressing wall scattering of FEL photons, and to prevent stray light generated in the PG2 beam line from reaching the particle detectors. About 3 m downstream from the interaction region, the photon pulses were sent onto a negatively biased Cu plate from which signals used to determine the arrival time of each photon pulse were derived. The spatial overlap of the two beams was verified by scanning a 1-mm-wide needle, inserted at 45° across the interaction region, thereby simultaneously blocking both beams.

To reduce the background from ions fragmenting after collisions with the residual gas (mainly H_2) and from photoelectrons generated by ionization of the residual gas, the pressure in the interaction region was kept at UHV conditions ($\sim 5 \times 10^{-10}$ mbar).

The data collection system was operated with a total rate of 20 Hz alternating between four different conditions, namely with (i) both ions and photon pulses in the interaction region, (ii) only ion pulses, (iii) only photon pulses, and (iv) neither ion nor photon pulses (dark counts). Thus, each condition repeated with a 5 Hz rate. By combining these measurements, background-corrected distributions of events from the ion-photon interaction only were obtained.

B. Ion-photon interaction

Figure 2 summarizes schematically the experimental setup around the interaction zone and the fragmentation detectors at TIFF. The photon and ion pulses cross inside a structure consisting of several electrodes [see Fig. 2(a)] that can be individually biased and that allow a detailed control of the electric field both parallel [left-right in Fig. 2(a)] and perpendicular [up-down in Fig. 2(a)] to the incoming ion beam. In the present experiment, these electrodes were used both to extract photoelectrons perpendicular to the plane spanned by the incoming ion and photon pulses [28] and to analyze fragment identities through uniformly biasing the complete interaction region [29].

To facilitate electron extraction, the voltages at the electrodes around the interaction zone were set to form an electric saddle point at the ion-photon crossing position as illustrated by the potential landscape shown in Fig. 2(b). Here, the saddle point potential was mainly established by the potentials applied to the electrodes C_1, C_2, U_0, and U_1. After extraction from the interaction zone, photoelectrons were guided vertically to either of the electron detectors (eDET 1 and eDET 2) at a distance $L_e = 0.142$ m through a retarding and focusing electric field shaped by the potentials applied to U_2 to U_9. The signals derived from the detectors eDET 1–2 were used to determine the electron times of flight (TOF) t_e relative to the ion-photon interaction time.

The atomic and molecular photofragments emerging from the interaction zone were detected on one of three multichannel plate (MCP) detectors (DET 1–3) shown in Fig. 2(a). Light fragments with sufficient transverse momentum release $\Delta p_F^{\perp}$ (H^0 and H^+) impinge on DET 1, heavy neutral fragments (OH^0) propagate to DET 2, and heavy charged fragments (OH^+ and H_2O^+) reach DET 3 after deflection in the electrostatic mirror. For a particle impacting on a fragment detector, i.e., DET i (i = 1,2,3), the time of flight t_i relative to the moment of interaction is registered, and for DET 1–2 also the transverse positions of impact (x_i, y_i) on the detector surface are determined. The predeflector, the electrostatic mirror, and DET 3 (used to analyze heavy charged fragments) were installed between the measurements performed at $\lambda_2 = 35.56$ nm and $\lambda_1 = 21.85$ nm, and thus were only available for the experiments at 21.85 nm.

To identify correlated events, i.e., particles resulting from the same fragmenting ion, coincidence analyses were applied to the data sets obtained with both ion and photon pulses present in the interaction region and considering those hits on DET 1–3 and eDET 1 that occurred for the same ion-photon crossing. Contributions from random coincidences in these analyses were determined by performing an identical analysis for uncorrelated events, obtained by combining signals from photon-ion crossings for the same order of respective micropulses but belonging to neighboring trains of FLASH pulses.

While this analysis is relatively uncomplicated for coincidences among fragments registered on DET 1–3, photoelectron spectroscopy poses an experimental challenge in the present type of experiments, since electrons must be detected on a significant background of electrons resulting from ionization of the residual gas [28] which can saturate the detection system. Thus, the data obtained under conditions for photoelectron spectroscopy, i.e., with the saddle point configuration of the interaction region [see Fig. 2(b)], were performed at a reduced FEL pulse energy (1–3 μJ/pulse).

C. Photofragment distributions

1. Photoions and -neutrals

The kinematics of the atomic and molecular fragmentation were analyzed by using the normalized coordinates introduced earlier [29,31]:

$$\begin{aligned} \rho_i &= r_i / \tilde{L}_i \quad (\text{DET 1 and DET 2}), \\ \tau_i &= t_i / (\tilde{L}_i / v_I), \end{aligned} \tag{1}$$

where $r_i = \sqrt{(x_i - x_0)^2 + (y_i - y_0)^2}$ is the transverse fragment impact position on DET i relative to the interaction point of the event. For events measured in coincidence on DET 1 and DET 2, the interaction point (x_0, y_0, z_0) is determined from the observed coordinates of the center of mass for each event separately [29,31]. Hence, the effective distance $\tilde{L}_i$ between the interaction point and the detector surface is derived for each event yielding $\tilde{L}_i = L_i - z_0$ with the measured distance L_i between the center of the interaction region and the detector surface (see Fig. 2). For events where only one fragment is registered with DET 1 or DET 2, the interaction point (x_0, y_0, z_0) is determined from the mean values of the single-particle distributions of these coordinates. Moreover, $v_I = \sqrt{2E_I/m_I}$ is the H_3O^+ ion velocity and E_I is

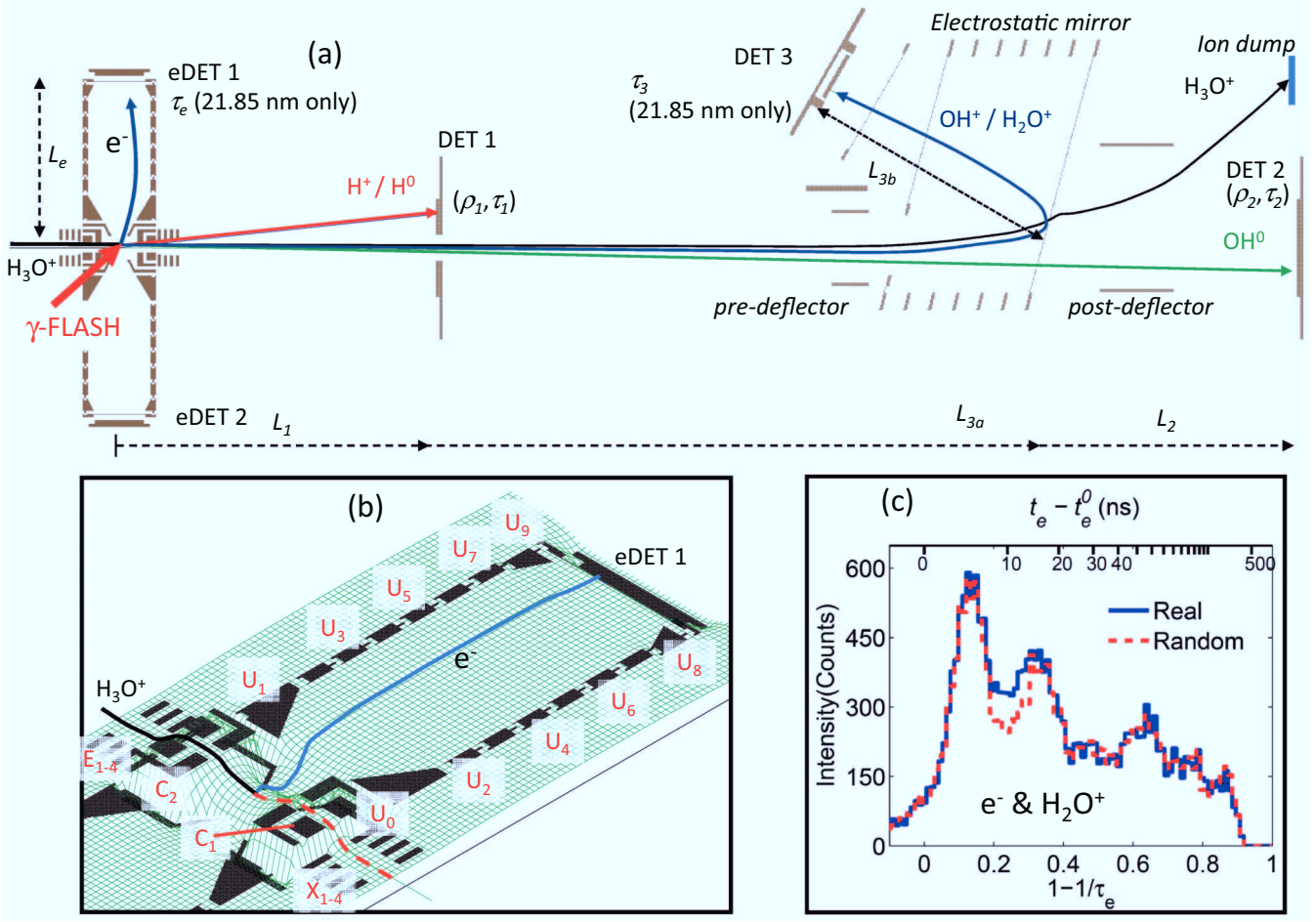

FIG. 2. (Color online) (a) Illustration of the interaction region at the TIFF experiment [25,29] at the FLASH facility [26,27]. For the experiment at 35.56 nm, DET 3, the predeflector and the electrostatic mirror were not installed. The dashed arrows indicate the distances from the center of the interaction region to eDET 1 ($L_e = 0.142$ m), to DET 1 ($L_1 = 0.263$ m), to DET 2 ($L_2 = 0.872$ m during measurement at 35.56 nm and $L_2 = 0.967$ m at 21.85 nm), as well as the horizontal distance from the interaction point to the most distant surface of the electrostatic mirror (L_{3a}) and upwards 150° to the plane defined by the surface of DET 3 (L_{3b}); this yields $L_3 = L_{3a} + L_{3b} = 0.975$ m. Solid lines show simulated trajectories for the parent H_3O^+ ion (black line) and heavy photofragments observed in the present experiment. The trajectory of a photoelectron extracted perpendicular to the ion and photon beams is also illustrated. (b) Potential landscape of the interaction zone when configured with an electric saddle point potential to extract photoelectrons to eDET 1–2. Here, the electrode were biased to $E_{1-4} = X_{1-4} = 0$, $C_{1-2} = -144$ V, $U_0 = 112$ V, $U_1 = U_{2-7} = -30$ V, and $U_{8-9} = 0$. The fronts of eDET 1–2 were biased to 100 V. (c) Photoelectrons registered on eDET 1 in coincidence with H_2O^+ fragments registered on DET 3 from correlated and noncorrelated ion-photon crossings (real and random coincidences, respectively). The spectra were obtained at 21.85 nm with reduced laser intensity (~2.9 μJ/pulse).

the kinetic energy in the interaction zone. With this definition, the dimensionless coordinates (ρ_i, τ_i) represents the transverse and longitudinal deflection of the fragment relative to a hypothetical nondeflected and nonretarded fragment emerging with the beam velocity.

When the interaction region is field-free or the photofragment is neutral ($q_F = 0$), the gain in transverse ($\Delta p_F^{\perp}$) and longitudinal ($\Delta p_F^{\parallel}$) momentum of a specific fragment due to the photofragmentation reaction is directly related to these coordinates through

$$\Delta p_F^{\parallel}/p_F = (\Delta p_F/p_F)\cos\theta_F = -(1 - 1/\tau_i) \qquad (2)$$

and

$$\Delta p_F^{\perp}/p_F = (\Delta p_F/p_F)\sin\theta_F = \rho_i/\tau_i, \qquad (3)$$

where $p_F = m_F v_I$ is the momentum of the undisturbed fragment. The total momentum release Δp_F and fragmentation angle θ_F relative to the laser polarization are then readily obtained as

$$\left(\frac{\Delta p_F}{p_F}\right)^2 = \left(\frac{\rho_i}{\tau_i}\right)^2 + \left(1 - \frac{1}{\tau_i}\right)^2 \qquad (4)$$

and

$$\tan\theta_F = -(\rho_i/\tau_i)/(1 - 1/\tau_i). \qquad (5)$$

Figure 3(a) shows the momentum image obtained from DET 1 at 35.56 nm using Eqs. (2) and (3) and furthermore illustrates the acceptance range of DET 1 and the resulting angular cut used for this particular experiment. The comparison to Fig. 8(a) of Ref. [25] shows the much improved statistics achieved in the present experiment in comparison to the earlier

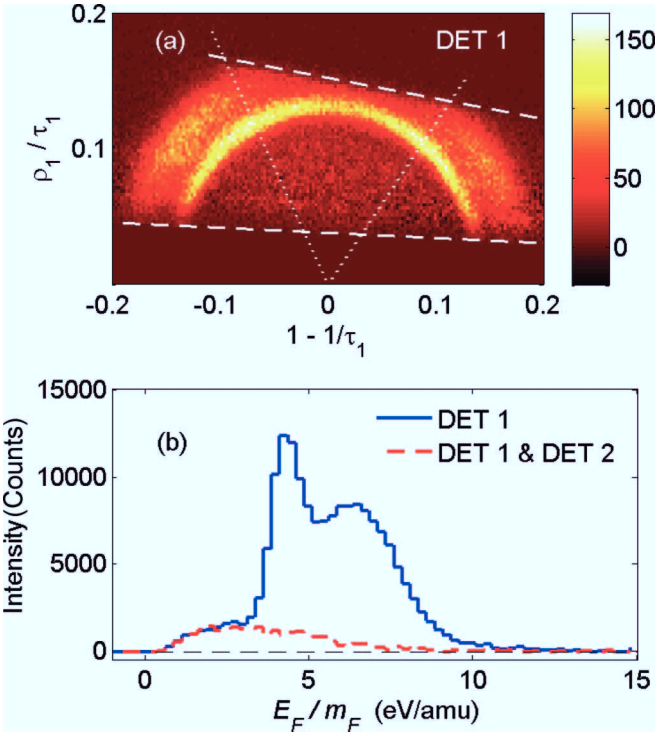

FIG. 3. (Color online) Analysis of light photofragments (H^0,H^+) from H_3O^+ obtained at $\lambda_2 = 35.56$ nm using DET 1 (see Fig. 2) and with field-free conditions in the interaction region. (a) Momentum image using the coordinates defined in Eqs. (2) and (3). The lower dashed line indicates the acceptance limit imposed by the central hole of DET 1 while the upper dashed line indicates the limit imposed by the finite size of DET 1. The dotted lines mark the angular cuts ($\theta_F \leqslant 60^\circ$ and $\theta_F \geqslant 130^\circ$) applied in the kinetic energy analysis. (b) Ratio of fragment kinetic energy and fragment mass obtained from Eq. (6) using the angular cut indicated in (a). The full (blue) line shows the distribution obtained for all fragments observed on DET 1 while the dashed (red) line shows the distribution for particles detected in coincidence with a neutral fragment on DET 2. The latter has been multiplied by a factor of 3.3 to facilitate the comparison of the two distributions, compensating for the finite efficiency of DET 2.

work, resulting from the at least sevenfold increase of the average FEL flux in the present experiment.

The momentum image acquired here clearly reveals two circular structures at larger radii in the ρ_1/τ_1 versus $1 - 1/\tau_1$ plane, which correspond to two distinct two-body fragmentation channels. Thus, for such channels, energy and momentum conservation necessitates the detection of only one fragment for a complete kinematic characterization. For each detected particle, its kinetic energy-to-mass ratio is evaluated directly as

$$\frac{E_F}{m_F} = \left(\frac{\Delta p_F}{p_F}\right)^2 \frac{E_I}{m_I}. \tag{6}$$

Figure 3(b) displays the distribution of E_F/m_F obtained for light fragments as recorded with DET 1 [full (blue) line]. This distribution is characterized by two peaklike structures centered at ~4.5 eV/amu and ~6.5 eV/amu, corresponding to circular features seen in Fig. 3(a).

Additionally, a broader structure is visible toward lower values of E_F/m_F in Fig. 3(b), corresponding to a flat low-intensity signal at lower radii in the momentum image. To identify the origin of this structure, Fig. 3(b) also shows the distribution of light photofragments obtained when requiring coincidence with one neutral particle registered on DET 2. As can be seen, the form of this distribution reproduces well the broad structure at low E_F/m_F, and hence this part of the total distribution originates mainly from photolysis of H_3O^+ leading in addition to a heavy neutral fragment.

2. *Photoelectrons*

The distribution of registered electrons is analyzed by comparison to a hypothetical electron that has absorbed the full photon energy (here $E_1 = 56.74$ eV) and which is emitted from the center of the interaction region directly vertically toward an electron detector (assuming the photoionized particle to be at rest) propagating through the electron spectrometer without any accelerating or decelerating fields. This electron carries a momentum of $p_e^0 = \sqrt{2m_e E_1}$ and reaches the detector after a time of $t_e^0 = L_e m_e / p_e^0 = 31.79$ ns, where L_e is the distance from the center of the interaction region to the detector (see Fig. 2). The observed electron times of flight are referenced to this hypothetical electron through the introduction of the dimensionless time $\tau_e = t_e/t_e^0$ and we present the data as a function of the reduced coordinate $1 - 1/\tau_e$ which explicitly emphasizes a shift relative to the reference electron. Similar to the definition of Eq. (2), this variable has an approximately linear relation to the electron momentum.

In the absence of fields, an electron emitted with a vertical momentum component of p_e^v (where $0 < p_e^v \leqslant p_e^0$) is observed with a reduced coordinate of

$$1 - 1/\tau_e = 1 - p_e^v / p_e^0 \quad \text{(field-free)}. \tag{7}$$

Evidently, p_e^v depends both on the fraction of the photon energy carried by the electron and the angle of emission, and under field-free conditions the distribution of the reduced coordinate $1–1/\tau_e$ is thus bound between $1–1/\tau_e = 0$, corresponding to electrons emerging with $p_e^v = p_e^0$, and $1–1/\tau_e = 1$, where the electrons emerge with zero momentum in the vertical direction. Without fields, however, only a small fraction of electrons actually reach eDET 1 or eDET 2 due to their finite sizes.

When biasing the electrodes around the interaction region to form an electric saddle point potential (see Fig. 2) and further biasing the subsequent drift region with accelerating or decelerating fields, *all* emitted photoelectrons can be guided to eDET 1 or eDET 2. Under such conditions, the reduced coordinate $1–1/\tau_e$ reflects the full laboratory momentum of the emitted electron; however, evidently the full three-dimensional momentum cannot be uniquely reconstructed from the single coordinate for an individual electron. In the presence of fields, the distribution of $1–1/\tau_e$ remains bound below $1–1/\tau_e = 1$, and for a particular photoelectron energy the distribution of $1–1/\tau_e$ is compressed and shifted characteristically of the chosen setting of the spectrometer fields; these fields can be adjusted to access different ranges of the photoelectron energy with variable resolution. It should be noted that the angular distribution of the emitted photoelectrons is also encoded in the particular shape of the resulting distribution of $1–1/\tau_e$. Explicit distributions of $1–1/\tau_e$ for fixed photoelectron energies are

considered in Monte Carlo simulations below (see Sec. III B 1), where also the Doppler shift of the electron momentum by the emission from the forwardly moving ion is included.

The electron signal was analyzed using photoion-photoelectron coincidence detection. Thus, coincidence was required between events occurring on DET 3 in narrow ranges of $1–1/\tau_3$, for example uniquely identifying H_2O^+ particles, and events on eDET 1. Figure 2(c) shows the observed spectrum of coincidence events between electrons and H_2O^+ ions obtained with eDET 1 under slightly retarding and focusing conditions of the drift region, corresponding to the potential landscape shown in Fig. 2(b). This coincidence spectrum contains both the photoelectron signal correlated with photoions and the uncorrelated background from random coincidence events through the ionization of rest gas by the FLASH laser. As mentioned previously (Sec. II B), we obtain the signal + background distribution from coincidence analysis of events from single micropulses in all pulse trains ("real coincidences"), while the background only is obtained from the same data sample by performing the coincidence analyses on the micropulses belonging to neighboring pulse trains ("random coincidences"). As seen in Fig. 2(c), the photoelectron signal correlated with photoions appears as a clear localized difference between the results from the two coincidence analyses on top of an otherwise identical structure. Hence, without a detailed model describing the origin of the background, the correlated photoelectron signal can be identified. The photoelectron spectrum resulting from the subtraction of the contribution from random coincidences and its comparison with simulated photoelectron spectra that give evidence about the energy of the emitted photoelectrons (and basically also contain information about their angular distribution) will be presented in Sec. III B 1 (Fig. 5).

III. RESULTS AND DISCUSSION

A. XUV photofragmentation channels

In the measurements at 21.85 nm, the added detector (DET 3) for heavy charged particles enables a multitude of fragment coincidence detections which allow access to an extensive picture of the XUV induced fragmentation channels. Figure 4 shows the relative longitudinal momenta as defined in Eq. (2) obtained at this wavelength from the fragment detectors DET 1–3 in a 3×3 matrix of TOF plots, where the plots for the total noncoincidence distributions form the diagonal and projections of the results from the various coincidence analyses appear as off-diagonal entries. For instance, Fig. 4 (11) shows the total distribution of light fragments observed on DET 1, being equivalent to a projection of the momentum image shown in Fig. 3(a) onto the horizontal axis.

Considering first the fragmentation channels leading to *heavy charged* fragments, the total distribution of particles registered with DET 3 is shown in Fig. 4 (33). From this distribution, H_2O^+ and OH^+ fragments are directly identified in two separate peaks as indicated. Additionally, no significant occurrence of O^+ particles can be identified and hence possible photofragmentations leading to O^+ containing channels are insignificant. The projected results of the coincidence analysis

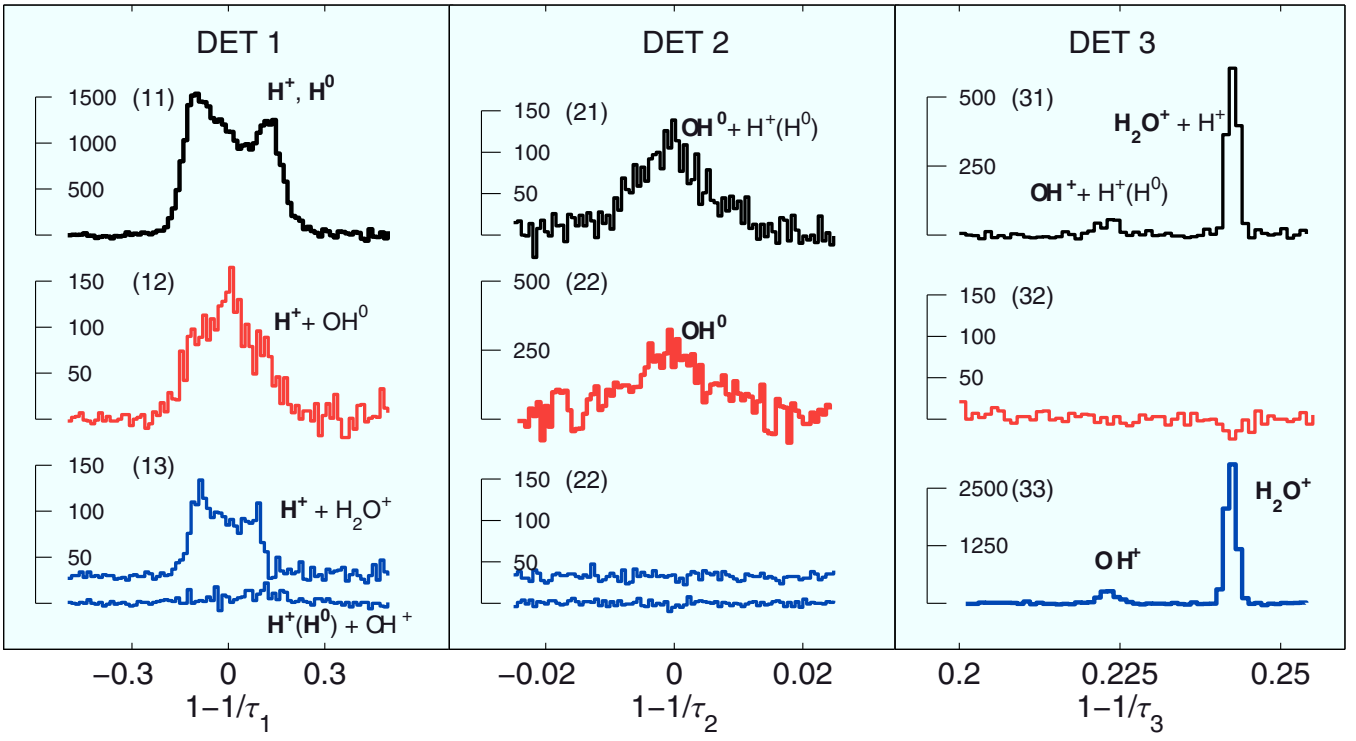

FIG. 4. (Color online) Identification of fragmentation channels and analysis of channel branching ratios in the photolysis of H_3O^+ at $\lambda_1 = 21.85$ nm. Distributions of fragment longitudinal momentum release in normalized coordinates [Eq. (2)] are shown for the events registered on DET 1–3 (see Fig. 2) under field-free conditions in the interaction region. The diagonal panels show the total noncoincidence distributions, while the off-diagonal panels display the distributions obtained after coincidence analysis between events on the three detectors where also the background of random coincidences has been subtracted.

between events on DET 1 and DET 3 are shown in Fig. 4 (13) and (31). It is evident that both the H_2O^+ and OH^+ fragments occur with at least one partner on DET 1. Separate measurements (not shown) were performed with the interaction region biased locally to 200–400 V, which allowed us to analyze the mass-to-charge ratio of the detected fragments [29,31]. These measurements revealed that most events registered with DET 1 stem from H^+ particles with a smaller contribution from H^0 particles (estimated to ~5–15 %), while no evidence for $H_2{}^+$ could be obtained. Collecting this information, we conclude that the XUV photofragmentation of H_3O^+ results mainly in two channels with a heavy charged fragment, namely $H_2O^+ + H^+$ and $OH^+ + H^+ + H^0$.

Heavy neutral particles were observed with DET 2 and their noncoincidence distribution is shown in Fig. 4 (22). As seen from the coincidence analysis viewed in Fig. 4 (12) and (21), the heavy neutral fragments occur in coincidence with light particles (H^+) registered with DET 1. By further analyzing coincidences with two particles (i.e., $2H^+$) on DET 1, and requiring momentum conservation, described explicitly in Sec. III B2, these neutral fragments were uniquely identified as OH^0, and hence the total fragmentation channel as $OH^0 + 2H^+$.

Summarizing, three main fragmentation channels are identified in the XUV photolysis of H_3O^+, namely

$$\begin{aligned} H_3O^+ + \lambda &\rightarrow e^- + H_3O^{2+} \\ &\rightarrow e^- + \begin{cases} H_2O^+ + H^+ & (a) \\ OH^0 + 2H^+ & (b) \\ OH^+ + H^+ + H^0 & (c). \end{cases} \end{aligned} \tag{8}$$

To determine the branching ratio between these fragmentation channels from the measured distributions shown in Fig. 4, we first formulate the following parametric equations for the total counts N_i observed with DET i ($i = 1$–3) in the identified peaks:

$$\begin{aligned} N_1 &= \varepsilon_1^a R_a + \varepsilon_1^b R_b + \varepsilon_1^c R_c, \\ N_2 &= \varepsilon_2^b R_b, \\ N_3^{OH^+} &= \varepsilon_3^c R_c, \\ N_3^{H_2O^+} &= \varepsilon_3^a R_a, \end{aligned} \tag{9}$$

where R_k is the number of processes actually occurring in channel k ($= a,b,c$), and ε_i^k is the probability for detecting channel k on DET i. These probabilities account for detector efficiencies, geometrical transmission losses, and fragment multiplicities (e.g., from an event of channel b or c, two particles are expected on DET 1). Considering the number of counts $N_{i\&j}$ observed in coincidence between pairs of detectors DET i and DET j, the additional equations

$$\begin{aligned} N_{1\&2} &= \varepsilon_1^b \varepsilon_2^b R_b = \varepsilon_1^b N_2, \\ N_{1\&3}^{OH^+} &= \varepsilon_1^c \varepsilon_3^c R_c = \varepsilon_1^c N_3^{OH^+}, \\ N_{1\&3}^{H_2O^+} &= \varepsilon_1^a \varepsilon_3^a R_a = \varepsilon_1^a N_3^{H_2O^+} \end{aligned} \tag{10}$$

are obtained.

From the measured values of N_i and $N_{i\&j}$ (Fig. 4), we are able to experimentally derive the detection probabilities $\varepsilon_1^a = 0.23 \pm 0.01$, $\varepsilon_1^b = 0.37 \pm 0.01$, and $\varepsilon_1^c = 0.27 \pm 0.02$. Further, the ratio between the cross sections for channels a and c is obtained independent of detection efficiency directly from $N_3^{H_2O^+}$ and $N_3^{OH^+}$ as

$$\frac{\sigma_{H_2O^+ + H^+}}{\sigma_{OH^+ + H^+ + H^0}} = 7.6 \pm 0.3. \tag{11}$$

To determine the ratio of channels a and b requires additionally the efficiency ε_2^b to be known, which cannot be derived by the coincidence procedure described above. An estimate of $1/\varepsilon_2^b$ can be obtained from the invoked scaling of the coincidence distribution in Fig. 3(b) to obtain the same intensity of the coincidence and noncoincidence distributions at low values of E_F/m_F. With a conservative estimate of $\varepsilon_2^b = 0.3 \pm 0.1$, we obtain

$$\frac{\sigma_{H_2O^+ + H^+}}{\sigma_{OH^0 + 2H^+}} = 4.0 \pm 1.3. \tag{12}$$

Finally, formulated directly as fragmentation branching ratios in XUV photolysis of H_3O^+, the results of Eqs. (11) and (12) are displayed in Table I. Considering the relatively large uncertainties on the photon pulse intensities and beam overlap in the present measurement, we refrain in this paper from stating an absolute value for the photoabsorption cross section. Absolute values for photolysis at 13.5 nm were estimated in a previous measurement [25].

TABLE I. Channel fragmentation branching ratios in the XUV photolysis of H_3O^+ at $\lambda_1 = 21.85$ nm.

Fragmentation channel	Branching ratio
$H_2O^+ + H^+$	$(72 \pm 4)\%$
$OH^0 + 2H^+$	$(18 \pm 6)\%$
$OH^+ + H^+ + H^0$	$(10 \pm 1)\%$

B. XUV photofragmentation pathways

Insight into the actual photofragmentation routes of the irradiated H_3O^+ ions producing the three identified channels [Eq. (8)] is here sought through the analysis of the photofragment momenta (including the electrons) and their kinetic energy release. The total energy balance for the ionization and dissociation process reads

$$E_\lambda + E_{vJ}^i = E_e + E_X + E_c + E_{vJ}^f, \tag{13}$$

where E_λ is the photon energy, E_e is the energy of the ejected photoelectron, E_X is the kinetic energy of the atomic and molecular dissociation fragments in the comoving center-of-mass frame, E_c is the electronic energy of the respective outgoing dissociation channel above the rovibrational ground state of H_3O^+, and $E_{v,J}^i$ and $E_{v,J}^f$ (where applicable) represent the rovibrational energies in the initial (i) and final (f) states, respectively.

For photofragments formed under field-free conditions in the interaction zone and impacting on DET 1 (H^+,H^0) or DET 2 (OH^0), the fragment energy-to-mass ratio (E_F/m_F) can be determined for each individual particle from the recorded impact time and position as described in Eq. (6). For heavy photoions, i.e., OH^+ and H_2O^+ on DET 3, we acquire, as explained earlier, in this experiment only the parameter $1–1/\tau_3$ [see Eq. (2)] which, due the deflection

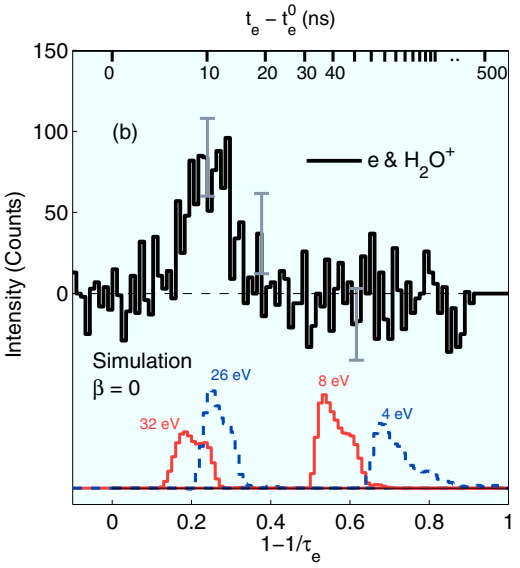

FIG. 5. (Color online) Distribution of photoelectrons emitted in the photolysis of H_3O^+ at $\lambda_1 = 21.85$ nm [upper full (black) curve], where the dimensionless coordinate $1 - 1/\tau_e$ is defined in Sec. II C2. The electrons were detected on eDET 1 in coincidence with H_2O^+ fragments detected with DET 3 (see Fig. 2). In the lower part, simulated distributions of photoelectrons emitted isotropically ($\beta = 0$) relative to the laser polarization and with different energies as indicated are shown.

in the electrostatic mirror, depends both on the transverse and longitudinal momentum of the fragment. Similarly, for each detected electron, we acquire the quantity $1–1/\tau_3$ [see Sec. II C2 and Fig. 2(c)], which depends both on the transverse and longitudinal momentum of the ejected electron, as a consequence of the extraction by the saddle point potential. Thus, while detailed kinematic event analyses are not possible in this measurement for the single-coordinate data from eDET 1 and DET 3, the full kinematic data of DET 1 and DET 2 allow very detailed information on the pathways for the two major fragmentation channels $H_2O^+ + H^+$ and $OH^0 + 2H^+$ to be extracted.

1. *Dicationic states accessed in the XUV*

A first aspect in the analysis of fragmentation pathways is the clarification of the electronic states of the formed dications. As indicated in Fig. 1, photoelectrons may be ejected from either inner ($2a_1$) or outer ($1e$ and $3a_1$) valence electron orbitals of the irradiated H_3O^+ ions.

Figure 5 shows the photoelectron spectra obtained in coincidence with H_2O^+ fragments at the shorter wavelength, $\lambda_1 = 21.85$ nm, where both inner and outer valence ionization are energetically allowed. To interpret the experimental distribution, Monte Carlo simulations were performed of photoelectrons emitted isotropically relative to the laser polarization (anisotropy parameter $\beta = 0$ [36]) from a 1 mm diameter beam of H_3O^+ of 4.2 keV kinetic energy, and assuming a longitudinal extension of the ion-photon overlap zone of 1 mm, mimicking closely the actual experimental situation. Simulated distributions, each based on 2000 electron trajectories, are shown for four representative photoelectron energies in the lower part of Fig. 5. Comparison of the observed spectrum and the results of the simulations clearly reveal that the observed distribution of electrons is consistent with photoelectron energies in the range of ~26–32 eV, while no evidence is seen for photoelectrons with lower energy. From the approximately known energies of photoelectrons from inner and outer valence orbitals [23] (see also Fig. 1), we conclude that only outer valence ionization contributes significantly to the fragmentation channel $H_2O^+ + H^+$. Thus, comparing the integrals of the spectrum in the ranges $1–1/\tau_e = 0.50–0.75$ and $1–1/\tau_e = 0.10–0.40$, where contributions from inner and outer valence ionization are expected, respectively, yields a ratio of -0.05 ± 0.11, consistent with the inner valence ionization being insignificant. Similar results (not shown) were obtained for electrons obtained in coincidence with particles registered with DET 1 (H^+, H^0), indicating that all three observed fragmentation channels [Eq. (8)] originate from outer valence ionization of H_3O^+.

From this finding, it also follows that the fragmentation routes are most likely independent of wavelength in the XUV regime. Thus, we here analyze further the fragmentation kinetics at the longer wavelength $\lambda_2 = 35.56$ nm where only outer valence ionization is possible, and we focus on the major channels ($H_2O^+ + H^+$ and $OH^0 + 2H^+$) based on measurements with DET 1–2, since we have obtained higher statistics and better resolution under these conditions. It should be stressed, however, that excitation of autoionizing resonances, e.g., as observed for the case of the isoelectronic Ne [37], of the monocation H_3O^+, for instance, below the $2a_1$ ionization threshold can potentially modify the fragmentation patterns in particular energy regions.

2. *Dissociation into $OH^0 + 2H^+$*

Events belonging to the fragmentation channel $OH^0 + 2H^+$ can be uniquely identified from a coincidence analysis requiring one hit on DET 2 and two hits on DET 1. In Fig. 6 the correlated distribution of relative longitudinal momenta for particles detected in this coincidence is shown for the experiment performed at $\lambda_2 = 35.56$ nm. Using the dimensionless coordinates defined in Eq. (2), the condition for momentum conservation corresponding to the $OH^0 + 2H^+$ channel explicitly takes the form

$$1 - 1/\tau_2 = -m_H/m_{OH}(2 - 1/\tau_{1(1)} - 1/\tau_{1(2)}). \quad (14)$$

Events fulfilling this condition and hence belonging to the fragmentation channel $OH^0 + 2H^+$ occur as a diagonal line in Fig. 6. Similarly, momentum conservation in the transverse directions is observed (not shown), and by selecting events where momentum conservation is fulfilled in all three directions, an almost background-free set of three-particle events belonging to $OH^0 + 2H^+$ is obtained. The total three-body kinetic energy release E_T [i.e., $= E_X$ in Eq. (13)] is then evaluated as

$$E_T = E_{H^+(1)} + E_{H^+(2)} + E_{OH^0}, \quad (15)$$

where the individual fragment energies are obtained from Eq. (6) and the identified fragment masses. Figure 7(a) displays the resulting distribution of kinetic energy release for the $OH^0 + 2H^+$ channel, where a broad distribution centered

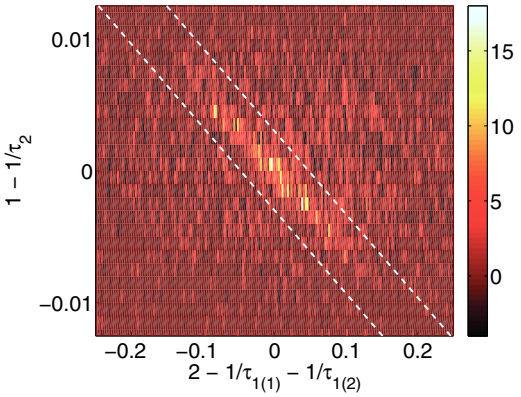

FIG. 6. (Color online) Relative longitudinal fragment momenta [see Eq. (2)] in the three-body break-up of H_3O^{2+} formed by ionization of H_3O^+ at 35.56 nm. The two-dimensional distribution of observed longitudinal momenta of fragments detected in coincidences with two hits on DET 1 and one hit on DET 2 (see Fig. 2) is shown. Sets of particles belonging to the fragmentation channel $OH^0 + 2H^+$ appear as a bright line corresponding to the condition for momentum conservation [Eq. (14)]. The white dotted lines indicate the range for which momentum conservation was considered fulfilled for the further analysis of kinetic energy release [Eq. (15)] and angular correlations [Eqs. (16) and (17)].

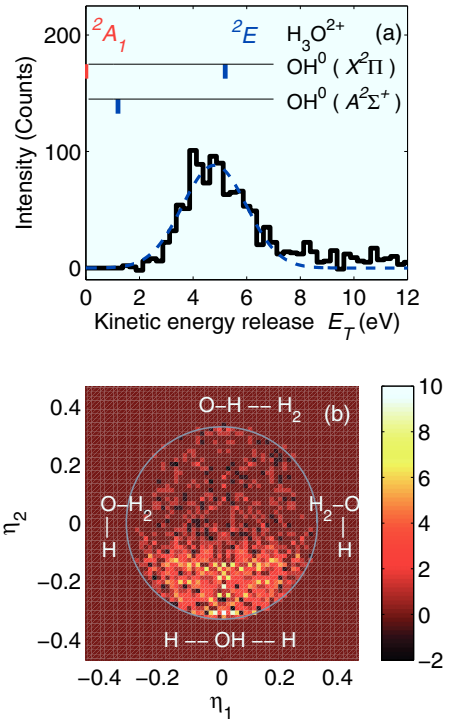

FIG. 7. (Color online) Photofragmentation of H_3O^+ at 35.56 nm leading to three-body break-up into $OH^0 + 2H^+$ obtained from coincidence detections of H^+ fragments with DET 1 and OH^0 fragments with DET 2 (see Fig. 2). (a) Total kinetic energy release (solid black line) E_T [Eq. (15)]. The dashed line (blue) shows a Gaussian fit to the distribution. The ladders above the experimental distribution show the estimated expected kinetic energy releases (see Fig. 1) for vertical transitions from the rovibrational ground state of H_3O^+ to states of H_3O^{2+} with subsequent dissociation into final states of $OH^0 + 2H^+$. (b) Dalitz plot representing the momentum sharing in the fragmentation process [Eqs. (16) and (17)].

around $E_T \sim 4.8$ eV is observed. A least-squares fit of a Gaussian profile to the distribution yields a mean energy of 4.8 ± 0.2 eV and a standard deviation of 1.2 ± 0.2 eV.

To identify the origin of the observed three-body fragmentation, we compare its energy range with the possible fragmentation channels after outer valence electron ionization as indicated in Fig. 1. Thus, the ladders above the experimental distribution indicate the expected mean kinetic energy releases for vertical transitions from the rovibrational ground state of H_3O^+ to states of H_3O^{2+} with subsequent dissociation into final states of $OH^0 + 2H^+$ implying energy conservation according to Eq. (13), i.e., with $E_\lambda - E_c$ at the orbital energies for outer valence electrons and for $E^i_{vJ} = E^f_{vJ} = 0$.

From this comparison, it appears that the only plausible assignment of the dissociation routes leading to the observed $OH^0 + 2H^+$ fragmentation is via the ^2E state of the dication dissociating into ground-state $OH^0(X^2\Pi)$, since dissociation from the $^2A_1$ state of the dication into excited states of OH^0 would lead to much lower energies than observed.

We interpret the width of the three-body kinetic energy distribution in Fig. 7(a), i.e., a full width at half-maximum of ~2.8 eV, as reflecting the extent (steepness) of the PES of the dication in the Franck-Condon region of H_3O^+.

As will be shown in Sec. III B3, the internal (rovibrational) excitation in the initial H_3O^+ ions should not exceed a few tenths of an eV. Hence, we can explain the shape of the distribution on the high-energy side only by an energy variation of the PES in the Franck-Condon region. Since it is unlikely that this broadening is strongly asymmetric, we also assign the shape on the low-energy side (where effects from the internal excitation of the OH^0 product could contribute) mainly to Franck-Condon broadening. On the other hand, it is interesting to note that the experimental distribution peaks at ~4.8 eV while a peak at ~5.2 eV would be expected from the calculated energy of the $1e$ orbital [23]. A likely reason for this difference is that the $OH^0(X\,^2\Pi)$ could on average be formed with about one quantum of vibrational excitation; the vibrational spacing for $OH^0(X\,^2\Pi)$ is ~0.46 eV [33]. Alternatively, the shift could indicate that the upper parts accessed on the ^2E potential energy surface of H_3O^{2+} dissociate mainly into other channels, i.e., here possibly $H_2O^+ + H^+$.

The complete experimental characterization of the fragments from the $OH^0 + 2H^+$ channel also allows us to analyze the angular correlation of the three emerging photofragments. For this purpose we use Dalitz coordinates [34] (η_1,η_2) adapted to the case of a three-body system with two identical particles [35]:

$$\eta_1 = \sqrt{\frac{m_I}{3m_{OH^0}}}\,\frac{E_{H^+(1)} - E_{H^+(2)}}{\sqrt{3}E_T} \tag{16}$$

and

$$\eta_2 = \frac{m_I}{3m_H}\,\frac{E_{OH^0}}{E_T} - \frac{1}{3}. \tag{17}$$

These coordinates are formed as linear combinations of fragment energies such that the coordinates are uniformly distributed in the case of a completely uncorrelated three-body break-up. Hence, structures in the Dalitz plot reveal angular

geometries characteristic of the dynamics of the dissociation. The mass-dependent factors used in Eqs. (16) and (17) result in a distribution confined by momentum conservation within a circle of radius 1/3 in the (η_1,η_2) diagram.

The Dalitz plot corresponding to the observed three-body dissociation of H_3O^{2+} is displayed in Fig. 7(b). Evidently, from the populated region of the ^2E state of H_3O^{2+}, dissociation with a near linear breakup with two protons leaving a central OH radical is dominating.

3. *Dissociation into $H_2O^+ + H^+$*

All three identified photofragmentation channels [Eq. (8)] contribute to the signal observed with DET 1 (see Fig. 3); however, the events registered there are by far dominated by the two-body dissociation into $H_2O^+ + H^+$. As shown explicitly in Fig. 3(b), the shape of the contribution from the strongest three-body channel ($OH^0 + 2H^+$) can be analyzed accurately from coincidences between events on DET 1 with DET 2. From the determined branching ratios, the effect of the three-body channel $OH^+ + H^+ + H^0$ on the spectrum in Fig. 3(b) is known to be small and to a first approximation its effect on the shape of the distribution can be assumed similar to the effect of the $OH^0 + 2H^+$ since similar kinetic energy releases are expected for the two channels (see Fig. 1). Hence, a reasonable approximation to the distribution of H^+ fragment kinetic energy in the $H_2O^+ + H^+$ channel can be obtained from the full distribution shown in Fig. 3(b) by simple subtraction of the three-body contribution from the channel $OH^0 + 2H^+$.

The two-body kinetic energy release E_k [$=E_X$ in Eq. (13)] is directly obtained from the identified single particles (H^+) as

$$E_k = \frac{\Delta p_F^2}{2\mu} = \left(\frac{\Delta p_F}{p_F}\right)^2 \frac{m_F}{m_I - m_F} E_I, \qquad (18)$$

where μ is the reduced mass of the two-body system. The resulting distribution of two-body kinetic energy is shown in Fig. 8. It should first be noted that the total width of the distribution is very similar to the width of the electron distribution (Fig. 5) in consistency with energy balance Eq. (13). Nevertheless, for a precise energetic analysis, the statistics and resolution in kinetic energy is more favorable for the fragment detection than for the obtained electron spectrum.

In more detail, the two-body kinetic energy distribution (Fig. 8) shows two peaklike structures: a relatively narrow peak centered at $E_k \sim 4.5$ eV and a wider peak at $E_k \sim 6.7$ eV. Quantitatively, the distribution is well represented as a sum of two Gaussian contributions, one centered at 4.54 ± 0.05 eV with a standard deviation of 0.41 ± 0.05 eV and another centered at 6.67 ± 0.05 eV with standard deviation of 1.48 ± 0.05 eV.

In analogy to the analysis for the three-body channel, we first seek to identify the origin of these structures by comparing their energy range with the possible fragmentation channels after outer valence electron ionization (Fig. 1). The ladders above the experimental distribution in Fig. 8 thus also indicate here the expected mean kinetic energy releases for vertical transitions from the rovibrational ground state of H_3O^+ to states of H_3O^{2+}. Considering the close matching of the mean fragmentation energy, the peak centered at $E_k \sim 4.5$ eV stems most likely from the $^2A_1$ state of H_3O^{2+} into $H_2O^+ + H^+$

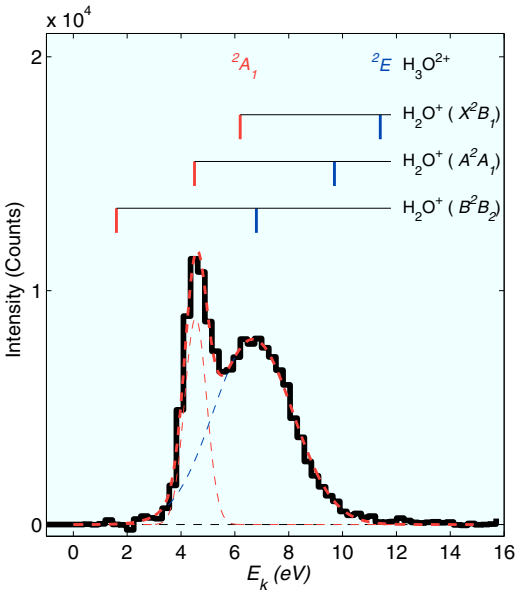

FIG. 8. (Color online) Photofragmentation of H_3O^+ at 35.56 nm leading to $H_2O^+ + H^+$ studied by momentum imaging of the H^+ fragment detected with DET 1 (Fig. 2). The black line shows the observed distribution of two-body kinetic energy releases for events with $\theta_F \leqslant 60^\circ$ and $\theta_F \geqslant 130^\circ$ [Eq. (5)]. The thick dashed line (red) shows a fit to the distribution with two Gaussian distributions, while the thin dashed lines (red and blue) show the contributions from the individual Gaussians. The ladders above the experimental distribution show the expected kinetic energy releases (see Fig. 1) for vertical transitions from the rovibrational ground state of H_3O^+ into states of H_3O^{2+} followed by dissociation into final states of the $H_2O^+ + H^+$ system.

with the water radical ion in its first excited state ($A\,^2A_1$). In addition, the small width of this peak indicates that the rotational and vibrational excitation in the final molecular state (H_2O^+) and also in the initial H_3O^+ ion do not exceed a few tenths of an eV. Also the variation of the dicationic PES over the Franck-Condon region is at most of similar size.

Similarly, the peak centered at $E_k \sim 6.7$ eV seems to originate from the ^2E state of H_3O^{2+} dissociating into H_2O^+ in the second excited state ($B\,^2B_2$). The mean energy expected for dissociation from the $^2A_1$ state of H_3O^{2+} into ground-state water ions could also be the origin of the peak at ~6.7 eV. However, this peak shows a symmetrical and much stronger broadening than that at ~4.5 eV, indicating a much larger Franck-Condon width and hence a different dicationic PES. Additionally, the width of the peak at ~6.7 eV is in fact similar to that of the observed kinetic energy distribution for the $OH^0 + 2H^+$ channel (Fig. 7), for which the assignment to dissociation from the ^2E state of H_3O^{2+} is certain.

With this understanding of the two-body kinetic energy spectrum, the very different widths of the two peaks at ~4.5 eV and ~6.7 eV in Fig. 8 illustrate that the $^2A_1$ PES is steeper than the ^2E PES of the dication in the Franck-Condon region accessed from the ground state of H_3O^+. The rather narrow peak at $E_k \sim 4.5$ eV with a half-width of only ~0.5 eV gives upper limits for the internal excitation of the parent H_3O^+ ion and for the H_2O^+ product in the relevant reaction channel.

More quantitatively, assuming similar angular distribution for the breakup via the $^2A_1$ and the ^2E state of the dication, the integrals of the two fitted Gaussian peaks in Fig. 8 clearly show that ionization through the ^2E dominates the two-body breakup channel. Thus, the ratio of the integrals of the fitted peaks is 3.2 ± 0.1, showing that ~76% of the two-body intensity arises from the ^2E state. This finding is consistent with the observed distribution of photoelectrons shown in Fig. 5, which despite its lower resolution indicates more intensity for photoelectron energies ~26 eV than ~32 eV.

IV. CONCLUSION

The crossed ion-photon beam setup TIFF installed at the free-electron laser FLASH has recently been enhanced to enable coincidence detection both for the photoelectrons [28] and for all emerging photofragments [29]. The present results represent a study in which these two features are exploited in combination for molecular ions.

Using this setup, our experiment yields detailed results on the XUV photoionization and fragmentation of H_3O^+, the involved dicationic states, and their fragmentation pathways. The results obtained using photoelectron detection demonstrate that outer valence ionization is completely dominant in the XUV photolysis of H_3O^+. Hence the fragmentation patterns of the resulting dications (H_3O^{2+}) can probably be assumed to be of a general nature in the complete XUV range, and likely also for other types of ionizing radiation such as electrons or fast (highly charged) ions.

Through the photoionization process, the potential energy curves for the $^1A_1$ and ^2E states of the dication H_3O^{2+} vertically above the ground state of the monocation are directly addressed. The dynamics of these dicationic states so far have not been investigated theoretically. Our experimental study indeed provides quantitative results that could form a sensitive test of theory for the dicationic states of H_3O^{2+}. First, we have identified only three major dissociation channels, namely $H_2O^+ + H^+$, $OH^0 + 2H^+$, and $OH^+ + H^+ + H^0$, and we determined explicitly their branching ratios (see Table I). Second, contributions from two cationic states and their state-specific fragmentation pathways have been identified (Table II). Thus, the ^2E state of the dication dominates the XUV photolysis, and a fraction near 55% of all events produces $H_2O^+ + H^+$ fragments via this state, while ~18% reach $OH^0 + 2H^+$ via this PES. Comparatively, the $^2A_1$ of the dication, dissociating into $H_2O^+ + H^+$, contributes a total fraction near 17%. The dicationic state responsible for the dissociation into $OH^+ + H^+ + H^0$ (total fraction ~10%) remains unidentified in the present study. Third, the main dissociation channel ($H_2O^+ + H^+$) leads to water radical ions in excited states. Explicitly, the $^1A_1$ state breaks up into the linear $\tilde{A}\,^2A_1$ state while the ^2E state dissociates to form the bent $\tilde{B}\,^2B_2$ state of H_2O^+. Fourth, for the fragmentation into the three-body channel $OH^0 + 2H^+$ we find OH^0 in its ground $X\,^2\Pi$ state and presumably on average with about one quantum of vibrational excitation. Finally, we demonstrate that the three-body breakup of this channel proceeds in a near-linear fashion with the two protons moving away from a central OH^0 fragment.

TABLE II. Identified state-resolved fragmentation routes of H_3O^+ after XUV photolysis.

State of H_3O^{2+}	Fragmentation channel	Branching ratio[a]
^2E	$H_2O^+(B\,^2B_2) + H^+$	$(55 \pm 5)\%$
^2E	$OH^0(X\,^2\Pi) + 2H^+$	$(18 \pm 6)\%$
$^2E/^2A_1$	$OH^+ + H^+ + H^0$	$(10 \pm 1)\%$
$^2A_1$	$H_2O^+(A\,^2A_1) + H^+$	$(17 \pm 2)\%$

[a]Derived assuming the same angular distribution of the two-body fragmentation channels ($H_2O^+ + H^+$) from the ^2E and $^2A_1$ states.

We expect that the present identification of the main fragmentation channels following H_3O^+ photoionization, based on coincidence detection of all photofragments, will help to understand the photochemistry of this ubiquitous ion under VUV and soft-x-ray irradiation in atmospheric [14,15] and astrophysical plasma [9–12]. In particular, channels yielding water radical cations H_2O^+ in electronically excited states are dominating, followed by a channel yielding neutral OH^0 radicals in their electronic ground state. Since no signs of inner valence ionization are found even clearly (>6 eV) above the corresponding energy threshold, the photolysis of H_3O^+ is dominated by outer valence ionization, and photochemistry models could likely consider the obtained fragmentation channels to provide the major contributions over a large part of the XUV and x-ray energies. Regarding quantum chemical modeling of the fragmentation via H_3O^{2+} potential energy surfaces, we expect that the detailed branching ratios obtained for the ground state ($^2A_1$) and first excited state (^2E) of the dication will help the theoretical understanding of this system. Future investigations of the XUV photolysis of H_3O^+ can be extended to yield also more precise absolute cross sections for the observed fragmentation routes.

ACKNOWLEDGMENTS

H.B.P. acknowledges support from the Lundbeck Foundation. This work has been supported by the Max-Planck Advanced Study Group at CFEL Hamburg and the Max-Planck Society. We sincerely thank the scientific and technical staff [27] at FLASH for their invaluable support.

[1] J. M. Hollis, E. D. Churchwell, E. Herbst, and F. C. DeLucia, Nature (London) **322**, 524 (1986).

[2] A. Wootten, J. G. Mangum, B. E. Turner, M. Bogey, F. Boulanger, F. Combes, P. J. Encrenaz, and M. Gerin, Astrophys. J. **380**, L79 (1991).

[3] R. Timmermann, T. Nikola, A. Poglitsch, N. Geis, G. J. Stacey, and C. H. Townes, Astrophys. J. **463**, L109 (1996).

[4] J. R. Goicoechea and J. Cernicharo, Astrophys. J. **554**, L213 (2001).

[5] M. Gerin *et al.*, Astron. Astrophys. **518**, L110 (2010).

[6] E. Gonzales-Alfonso *et al*., Astron. Astrophys. **550**, A25 (2013).
[7] D. Smith, Chem. Rev. **92**, 1473 (1992).
[8] J. Lequeux and E. Roueff, Phys. Rep. **200**, 241 (1991).
[9] A. Sternberg and A. Dalgarno, Astrophys. J. **99**, 565 (1995).
[10] D. J. Hollenbach and A. G. G. M. Tielens, Annu. Rev. Astron. Astrophys. **35**, 179 (1997).
[11] D. J. Hollenbach and A. G. G. M. Tielens, Rev. Mod. Phys. **71**, 173 (1999).
[12] P. Stäuber, S. D. Doty, E. F. van Dishoeck, and A. O. Benz, Astron. Astrophys. **440**, 949 (2005).
[13] D. J. Hollenbach, M. J. Kaufman, E. A. Bergin, and G. J. Melnick, Astrophys. J. **690**, 1497 (2009).
[14] R. P. Wayne, *Chemistry of Atmospheres*, 3rd ed. (Oxford University Press, New York, 2000).
[15] M. Larsson, W. D. Geppert, and G. Nyman, Rep. Prog. Phys. **75**, 066901 (2012).
[16] T. J. Sears, P. R. Bunker, P. B. Davies, S. A. Johnson, and V. Spirko, J. Chem. Phys. **83**, 2676 (1985).
[17] J. Tang and T. Oka, J. Mol. Spectrosc. **196**, 120 (1999).
[18] T. Furuya, S. Saito, and M. Araki, J. Chem. Phys. **127**, 244314 (2007).
[19] A. Miani, A. Beddoni, J. Pesonen, and L. Halonen, Chem. Phys. Lett. **363**, 52 (2002).
[20] X. Huang, S. Carter, and J. Bowman, J. Chem. Phys. **118**, 5431 (2003).
[21] T. Rajamäki, A. Miani, and L. Halonen, J. Chem. Phys. **118**, 10929 (2003).
[22] F. Di Giacomo, F. A. Gianturco, F. Raganelli, and F. Schneider, J. Chem. Phys. **101**, 3952 (1994).
[23] R. C. Raffenetti, Chem. Phys. Lett. **46**, 513 (1977).
[24] A. Faure and J. Tennyson, J. Phys. B **35**, 1865 (2002).
[25] H. B. Pedersen *et al*., Phys. Rev. A **80**, 012707 (2009).
[26] W. Ackermann *et al*., Nat. Photon. **1**, 336 (2007).
[27] K. Tiedtke *et al*., New J. Phys. **11**, 023029 (2009).
[28] L. S. Harbo, A. Becker, S. Dziarzhytski, C. Domesle, N. Guerassimova, A. Wolf, and H. B. Pedersen, Phys. Rev. A **86**, 023409 (2012).
[29] H. B. Pedersen *et al*., Phys. Rev. A **87**, 013402 (2013).
[30] M. Martins *et al*., Rev. Sci. Instrum. **77**, 115108 (2006).
[31] H. B. Pedersen, L. Lammich, C. Domesle, B. Jordon-Thaden, O. Heber, J. Ullrich, R. Treusch, N. Guerassimova, and A. Wolf, Phys. Rev. A **82**, 023415 (2010).
[32] T. Koopmans, Physica (Amsterdam) **1**, 104 (1934).
[33] National Institute of Standards and Technology database, http://www.nist.gov.
[34] R. H. Dalitz, Phys. Rev. **94**, 1046 (1954).
[35] D. Strasser, L. Lammich, H. Kreckel, M. Lange, S. Krohn, D. Schwalm, A. Wolf, and D. Zajfman, Phys. Rev. A **69**, 064702 (2004).
[36] J. Cooper and R. N. Zare, J. Chem. Phys. **48**, 942 (1968).
[37] K. Schulz, M. Domke, R. Puttner, A. Gutierrez, G. Kaindl, G. Miecznik, and C. H. Greene, Phys. Rev. A **54**, 3095 (1996).